Bioactive Materials 5 (2020) 891–901

Contents lists available at ScienceDirect

Bioactive Materials

journal homepage: http://www.keaipublishing.com/biomat

In-vitro biomineralization and biocompatibility of friction stir additively manufactured AZ31B magnesium alloy-hydroxyapatite composites

Yee-Hsien Ho[a], Kun Man[b], Sameehan S. Joshi[a], Mangesh V. Pantawane[a], Tso-Chang Wu[a], Yong Yang[b], Narendra B. Dahotre[a,*]

[a] Laboratory for Laser Aided Additive and Subtractive Manufacturing, Department of Materials Science and Engineering, University of North Texas, 1150 Union Circle 305310, Denton, TX, 76203-5017, USA
[b] Department of Biomedical Engineering, University of North Texas, 1150 Union Circle 305310, Denton, TX, 76203-5017, USA

ARTICLE INFO

Keywords:
Friction stir processing
Magnesium alloy
Hydroxyapatite
Additive manufacturing
Biomineralization
Contact angle measurement
Blood compatibility
Cell culture

ABSTRACT

The present study aims to evaluate effect of hydroxyapatite (HA, $Ca_{10}(PO_4)_6OH_2$), a ceramic similar to natural bone, into AZ31B Mg alloy matrix on biomineralization and biocompatibility. The novel friction stir processing additive manufacturing route was employed to fabricate Mg-HA composites. Various HA contents (5, 10, 20 wt %) were incorporated into Mg matrix.

Microstructural observation and chemical composition analysis revealed that refined Mg grains and dispersion of HA particles at micro/nanoscales were achieved in Mg-HA composites after the friction stir processing. The biomineralization evaluation were carried out using immersion experiments in simulated body fluid followed by mineral morphology observation and chemical composition analysis. The wettability measurements were conducted to correlate the biomineralization behavior. The results showed improvement in wettability and bone-like Ca/P ratio in apatite deposit on the composites compared to as-received Mg. In addition, the increase of blood compatibility, cell viability and spreading were found in the higher HA content composites, indicating the improved biocompatibility. Therefore, friction stir processed Mg-20 wt%HA composite exhibited the highest wettability and better cell adhesion among other composites due to the effect of increased HA content within Mg matrix.

1. Introduction

Biodegradable Magnesium (Mg) and its alloys are candidate metallic materials for consumable bioimplant application due to their non-toxic oxide product, biocompatibility, and similar elastic modules to human bone [1–3]. Mg alloys are suitable to manufacture stents and plates for temporary function of mechanical support to a fracture bone until they completely dissolute and be absorbed by the surrounded tissue, without secondary surgical procedure requirement [4,5]. Nevertheless, Mg-base implants suffer severe corrosion because of their low electrochemical potential in a physiological environment with rich Cl ions content [2,6]. In addition, the presence of secondary phases in Mg leads galvanic coupling effects and aggravate localized pitting corrosion [7,8]. The rapid corrosion of Mg alloys not only deteriorates their mechanical integrity but also releases severe hydrogen gas upon corrosion, causing implant failure and cell detachment on implant surface before the bone can fully heal [2]. To address this issue, diverse methods such as alloying, surface coating, and surface composite are used to overcome corrosion issue as well as improve apatite formation and cell adhesion on Mg surface. In present, the conventional alloying elements for Mg biomaterials are Aluminum (Al), Zinc (Zn), Calcium (Ca), Manganese (Mn), Zirconium (Zr), and rare earth (RE) [9,10]. Among these elements, Al and RE are noticed as neurotoxicant and hepatotoxicity to human, respectively [11,12]. Their dissolved ions can accumulate in human metabolic system and eventually may induce diseases and organ damage such as Alzheimer, dementia, and hepatitis [11,12]. Hence, the added content of these metallic elements needs to be carefully controlled for the sake of health safety. Besides that, ceramic materials such as bioglass and calcium phosphate base (Ca–P) ceramic are also favorable composite materials for medical applications due to their excellent biocompatibility, rapid biomineralization, and protein absorption [13–15]. Especially Ca–P is the major composition in human bone, and can induce osteoconductive process, recruitment of immature cells and the stimulation of these cells to develop into

Peer review under responsibility of KeAi Communications Co., Ltd.
* Corresponding author.
E-mail address: Narendra.Dahotre@unt.edu (N.B. Dahotre).

https://doi.org/10.1016/j.bioactmat.2020.06.009
Received 30 April 2020; Received in revised form 8 June 2020; Accepted 12 June 2020

preosteoblasts [16]. Therefore, Ca–P is suitable for surface coating or composites of metallic base implants with improvement of biocorrosion and biocompatibility. On account of this, the investigation of bioceramic incorporated in Mg-base implant has grown significantly in the area of biomaterials.

Hydroxyapatite (HA, $Ca_{10}(PO_4)_6OH_2$) is one of the promising Ca–P minerals that has similar chemical composition and crystallographic structure to natural bone [17]. Owing to its ostecoconductive behavior, HA can form tight bonding with bone tissues in short period of time. Furthermore, the growth of apatite mineral phase on HA during implantation not only enhances osteoinduction but also reduces degradation rate of the substrate [18]. In light of this, HA is conceived to be a promising material for orthopedic applications of Mg alloy. HA surface coating on Mg substrate to improve biocorrosion resistance and biocompatibility is a well known technique [18–22]. Nevertheless, due to the lack of binding of coating with the substrate, the degradation behavior of Mg substrate depends on the quality of surface coating. The presence of defects such as cracks and porosity between the coating layer and substrate can act as anodic sites and trigger corrosion reaction in underlaid substrate, leading the failure of coating before the stabilization of apatite layer. Due to the weak bonding reaction and large thermal properties variation between Mg matrix and HA ceramic particle it is a challenge to produce defect free coating layer. Hence, a fabrication of Mg/HA composite can be an alternate solution to avoid these issues.

Several techniques such as powder metallurgy, melting and extrusion, high-frequency induction heat sintering, laser surface processing, and friction stir process (FSP) have been utilized to fabricate Mg/HA composites [21,23–28]. This study explored fabrication of AZ31B-HA surface composites via friction stir additive manufacturing. The major advantages of FSP are to produce refined grain structure in Mg matrix and to disperse HA particle into Mg matrix [29,30]. During FSP, a rotating tool consisting of a cylindrical shoulder and small pin is inserted into Mg surface. Such stirring action between rotating tool and matrix generates localized heat and causes material matrix soften, resulting in mechanical mixing of the ceramic HA particles with it. Furthermore, due to a significant plastic deformation caused by the tool rotating movement, dynamic recrystallization is induced in the processing region, hence assisting in reducing average grain size of material matrix [27,30]. The current investigation involved addition of incremental amounts of HA particles into the matrix of AZ31B Mg alloy. Due to the low Al contain, AZ31B Mg alloy is considered as biocompatible material in Al–Zn series [22]. The present study also investigated microstructure and phase evolution in additively produced AZ31B Mg-HA surface composites, henceforth referred as Mg-HA surface composites. Moreover, effects of microstructure evolution on surface wettability, biomineralization behavior, blood compatibility, and cell viability of these FSP surface composites were explored and compared with untreated AZ31B Mg alloy in simulated body fluid (SBF) environment. In addition, the corresponding microstructure evaluation, mineral phase surface morphology, and chemical composition were studied.

2. Experimental procedures

2.1. Materials and sample preparation for additive FSP

The sheets of 20 mm × 127 mm x 2.3 mm (width x length x thickness) were cut from commercial AZ31B Mg alloy sheets (composition: 3.0 wt% Al, 1.0 wt% Zn, 0.5 wt% Mn, and Mg balance) for this study. Pure hydroxyapatite powder (97.9–99.9% ACROS ORGANICS Inc.) was used to produce AZ31B Mg-HA metallic matrix composites. The average HA particle size was 10 μm. Three different weight percentages of HA powder (5 wt%, 10 wt%, and 20 wt%) were employed with respect to the fixed weight of the AZ31B Mg plates. Fig. 1 shows the schematic isometric view of packed sample. The detail of packing process had been described in the previous literature [21,31].

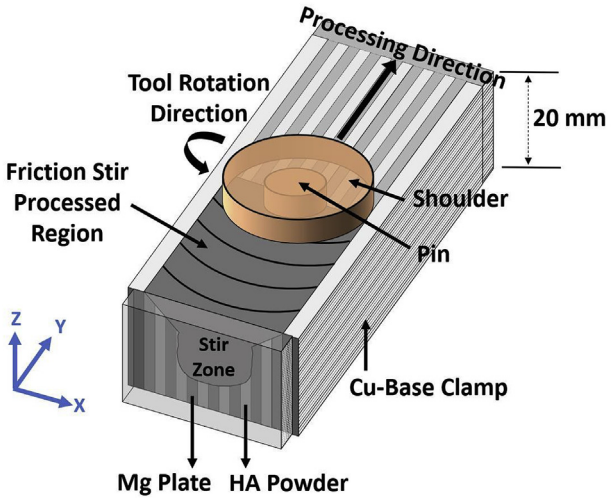

Fig. 1. Schematic of (a) isometric view of the FSP, (b) top view of the FSP, (c) side view of the FSP procedures followed in the current work.

2.2. Friction stir processing

The FSP was employed to incorporate and disperse HA powder into AZ31B Mg matrix as show in Fig. 1. The rotation FSP tool included a threaded pin (6 mm in diameter and 6 mm in thickness) and a shoulder (16 mm in diameter) made of nitrided high-speed steel. The rotating tool was traversed along the traverse axis of the sample with a linear speed of 30 mm/min, rotation speed of 900 RPM, and 3° traverse angle. After FSP tool traversed over the processed region it went back to the original starting point without stirring the sample and the sheet being processed was rotated 180°. This process was repeated 10 times to ensure the HA powder was uniformly mixed into Mg matrix during FSP.

2.3. Phase identification

Phases formed in the FSP Mg-HA composites and as-received Mg were characterized by X-ray diffraction (XRD, Rigaku III Ultima X-ray diffractometer) with Cu Kα radiation (wavelength = 0.15418 nm). The XRD system was operated at 40 kV and 44 mA in a 2θ range of 20–50° using a step size of 0.025° and a scan rate of 1°/min. The XRD analysis software JADE was utilized to identify phases in the XRD spectrum. The phases present in the resulting pattern were identified by comparing the XRD spectra with standard International Center for Diffraction Data (ICDD) files obtained from the Joint Committee of Powder Diffraction Standards (JCPDS).

2.4. Microstructure

In the present work, the microstructure and elemental distribution within as-received Mg and the stir zone of FSP Mg-HA composites were examined by the scanning electron microscope (SEM) equipped with Energy-Dispersive X-ray Spectroscopy (EDS) (FEI Quanta 200 environmental ESEM). In order to extract the FSP stir zone of Mg-HA composites, the samples were cut into 6 mm × 6 mm x 5 mm coupons using slow speed diamond saw. All FSP Mg-HA composites and as-received Mg coupons were mounted in epoxy prior to SiC paper polishing (grit size:600 to 1200). The following cloth polishing was carried out by using aluminum oxide (Al_2O_3) powder (particle size ranging from 1 to 0.03 μm) to remove the surface scratches from paper polishing. The finished coupons were then ultrasonically cleaned with methanol for 30 min prior to atmospheric drying. To reveal the microstructural features, all polished coupons were etched in the mixture of 5 mL acetic acid, 6 g picric acid, 10 mL H_2O, and 100 mL ethanol (95%) for approximately 5 s by immersion etching. The specific microstructural

attributes in various SEM micrographs were then quantified using ImageJ™ software. In addition, Philips 420 Transmission Electron Microscope (TEM) was utilized to gain the insight into fine scale to study the microstructure evolution of FSP Mg-HA composites.

2.5. Contact angle measurement

The surface wettability evaluation of as-received Mg and all FSP Mg-HA composites were carried out by contact angle measurement using CAM-Plus^R contact angle goniometer (Cheminstruments Inc. Fairfiled, OH), equipped with fiber optic light source. A liquid droplet of volume 3 μL (drop diameter of 2 mm) was placed on the thoroughly cleaned sample by a hypodermic syringe. The liquid droplet was placed on the surface for approximately 10 s to stabilize before the reading was taken. The measurement was carried out at room temperature (25.0 °C) and a minimum of ten contact angle readings were taken on each testing surface to minimize errors in the measurement. In order to eliminate the error associated with the arbitrary tangential alignment, the contact angle was measured based on the patented half angle method (US Patent 5268733).

According to the Van Oss approach [32], the surface energy can be calculated by the following Equation:

$$1 + \cos\theta_{\gamma L} = 2\{\sqrt{\gamma_S^{LW}\gamma_L^{LW}} + \sqrt{\gamma_S^{+}\gamma_L^{-}} + \sqrt{\gamma_S^{-}\gamma_L^{+}}\} \quad (1)$$

In this equation θ is the contact angle of liquid and solid, γ is the surface energy, it can be divided into the Lifshitz - van der waals surface (γ^{LW}) and Lewis acid-base surface energy (γ^{AB}) components as in the following equations:

$$\gamma = \gamma^{LW} + \gamma^{AB} \quad (2)$$

$$\gamma^{AB} = 2\sqrt{\gamma^{+}\gamma^{-}} \quad (3)$$

Here γ^+ is the Lewis acidic or the electron-acceptor components, γ^- is the Lewis basic or the electron-donor component. The subscripts S and L represent solid and liquid, respectively. To solve three unknown components (γ_S^{LW}, γ_S^+, and γ_S^-) in Equation (1), three well characterized test liquids were required. One non-polar liquid (1-Bromonaphthalene) and two polar liquids (Water and Formamide) were used in the test. The surface energy components of these three liquids were listed in Table 1 [33,34]. In order to correlate the surface energy calculations to wettability evaluation of as-received Mg and all FSP Mg-HA composites, the contact angle measurements were also performed for simulated body fluid (SBF) solution. The preparation process of SBF had been described in the previously published literature [35].

2.6. Biomineralization evaluation

To predict the cell integration, all FSP composites and as-received Mg were cut into coupon of 5 mm × 5 mm and mounted in epoxy for *in-vitro* SBF immersion. The test coupons were immersed in SBF solution at constant temperature (36.5 °C). In order to avoid gravity effect on mineralization behavior, all immersed coupons were vertically placed in SBF. The volume of SBF for the immersion test was determined by $V_s = S_a/10$, where V_s is the volume of SBF (mL) and S_a is the surface area of the coupon (mm^2). The immersed time for this measurement were 1, 4, 8, and 12 days, and the SBF solution was refreshed every 24 h to maintain pH of 7.4. The immersed coupons were removed from SBF and rinsed with deionized water and then dried in ambient atmosphere. The mineralized surface morphology observation was conducted by SEM and EDS, and the element analysis of the mineralized surface was conducted by X-ray photoelectron spectroscopy (XPS, VersaProbe$^{T\ M}$ 5000). The monochromatic X-ray beam source at 1486.6 eV, 49.3 W, and 200 μm beam diameter was operated to scan upon the mineralized surface. The vacuum condition was 5 × 10^{-6} Pa for the analysis.

2.7. Platelet adhesion

The samples were cut into 5 mm × 5 mm x 2 mm (width x length x thickness) using a slow speed diamond saw. The samples were placed in a 48-well plate and 60 μL of platelet rich plasma (PRP) (Zen-Bio, US) was placed over each sample surface and incubated at 37 °C for 1 h. The samples were subsequently rinsed gently with PBS to remove the non-adherent platelets, and fixed with 4% paraformaldehyde (PFA, Sigma-Aldrich, US) and 2% glutaraldehyde solution (Fisher Chemical, US) at room temperature for 2 h, followed by dehydration with gradient ethanol (30%, 50%, 70%, 90%, and 100%) and then hexamethyldisilazane (HMDS), each step for 10 min. The samples were stored in a desiccator and sputter-coated with gold before SEM observation. The adhered platelets were counted from at least six SEM images at 2000x magnification for each sample.

2.8. Hemolysis test

Healthy human blood containing 3.8% sodium citrate (Zen-Bio, US) was diluted with 0.9% sodium chloride solution (4:5 ratio by volume). The samples were immersed in 15 mL centrifuge tubes containing 9.8 mL 0.9% sodium chloride solution and incubated at 37 °C. After 30 min, 200 μL of diluted blood was added to each tube and incubated at 37 °C for 1 h. Meanwhile, 200 μL of diluted blood was added to 9.8 mL deionized water and 0.9% sodium chloride solution, respectively, as positive and negative controls. After centrifuging the tubes at 3000 rpm for 5 min, the supernatants were collected and the absorbance (A) was measured at wavelength of 545 nm in a Cytation 5 Cell Imaging Multi-Mode Reader (BioTek, US). The hemolysis ratio (HR) was calculated by the following equation:

$$HR(\%) = (A_{sample} - A_{negative})/(A_{positive} - A_{negative}) \times 100 \quad (4)$$

2.9. MTT assay and cell counting

The samples were placed in a 48-well plate and sterilized with UV for 30 min followed by rinsing with PBS buffer. The murine calvarial pre-osteoblasts (MC3T3-E1, ATCC CRL-2593, US) were seeded in the plate at a density of 10,000/cm^2 and cultured for 1 and 7 days in 37 °C and 5% CO_2.

The cell biocompatibility was examined by conducting MTT assay (Life Technologies, US). After cultured for the predetermined day, the test coupons were transferred to a 96-well plate, and filled with 100 μL of fresh culture medium and 10 μL of 12 mM MTT stock solution in each well.

Meanwhile, 10 μL of the MTT stock solution was added to 100 μL of medium alone in a well as negative control. The plate was then

Table 1
Surface energy components of the standard liquids (unit:mJ/m^2).

Liquids	Total Surface Energy γ	Van Der Waals Surface Energy γ^{LW}	Lewis Acidic Surface Energy γ^+	Lewis Acidic Surface Energy γ^-
1-Bromonaphthalen	44.4	44.4	0	0
Formamide	58.0	39.0	2.28	39.6
Water	72.8	21.8	25.5	25.5

incubated at 37 °C for 4 h. Subsequently, the medium was removed from the wells and 50 μL of DMSO was added to each well and mixed thoroughly with pipette. After incubation at 37 °C for 10 min, each well was mixed again, and the medium was transferred to a new well and absorbance was read at wavelength of 540 nm in plate reader. Each processed condition was repeated 3 times.

The cell biocompatibility was also quantified by counting adherent cells. After cultured for 1-day or 7-day, the coupons were transferred to 96-well plate and rinsed with PBS buffer solution. 100 μL of 0.05% Trypsin/EDTA was added to each well to release the cells from the surface. Total cell count for each sample was determined using countess II automated cell counter (Invitrogen, US). The cell counting was repeat 3 times for each processed condition.

2.10. Immunofluorescence staining

The MC3T3 cells at a seeding density of 10,000/cm^2 were cultured on the substrates for 1 day and fixed for immunofluorescence observation as follows. The samples were rinsed gently with PBS and fixed with 4% PFA solution for 15 min at room temperature. Subsequently, the samples were rinsed 3 times with PBS and blocked for 1 h at room temperature using PBST solution (PBS supplemented with 0.2% Triton X-100) containing 0.03 g/mL bovine serum albumin (BSA, Sigma-Aldrich, US) and 0.1% goat serum (Sigma-Aldrich, US). The samples were then incubated with Alexa Fluor 488 phalloidin (1:200, Life Technologies, US) for 2 h at room temperature. After rinsed 3 times with PBS, the samples were mounted using ProLong Gold Antifade Reagent with 4,6-diamidino-2-phenylindole (DAPI, Life Technologies, US). Images were obtained using Nikon Ti eclipse fluorescence microscope.

2.11. Cell morphology observation

The MC3T3 cells at a cell seeding density of 10,000/cm^2 were cultured on the samples for 1 day and prepared for SEM observation by following the same procedure as platelet adhesion study that was described in Section 2.7.

2.12. Statistical analysis

All collective data from cell culture was mean as ± standard errors of at least triplicates. The statistical significances were analyzed based on two-tailed *t*-test, by using Prism 8 (GraphPad software, US), with the significance level defined as $p < 0.05$.

3. Results and discussion

3.1. Phase identification

The XRD analysis revealed that α-Mg (ICCD #:00-025-0821) was the major phase in as-received Mg and all FSP Mg-HA composites (Fig. 2). The presence of HA peaks (ICCD #:01-000-7087) are present in all FSP Mg-HA composites. The intensity of HA peaks ((202) and (302)) increased with increase in added HA content (encircled region in Fig. 2), indicating that not only the HA powder was successfully incorporated into Mg matrix but also the amount of HA content can be tailored via FSP. Furthermore, FSP Mg-HA composites had relatively broader α-Mg peaks than as-received Mg. Our previous study showed that this peak broadening can be attributed to the refined grain structure within the matrix after FSP [21]. The similar observation was found in HA (202) and (302) peaks, indicating the particle size was refined [21]. This preceding analysis again verified that HA powder was successfully incorporated into Mg matrix via FSP. The following section will describe the observation of HA particle distribution within Mg matrix via scanning electron microscope.

3.2. Microstructure

The secondary electron (SE) mode SEM images revealed the equiaxed grain structure in case of as-received Mg (Fig. 3) and an equiaxed refined grain matrix with secondary phase particles embedded within stir zone for all FSP Mg-HA composite (Fig. 3). The measurement indicated that after FSP the Mg grain size reduced from 7.7 ± 1.8 μm to range of 3.5 to 2.2 μm. This observation supported that the Mg peaks in the XRD spectra of FSP Mg-HA composites became broader compared to that of as-received Mg. It has been reported that the evolution of grain refinement during FSP was attributed to the occurrence of dynamic recrystallization [36]. Moreover, the backscatter electron (BSE) mode and EDS elemental mapping analysis is presented in the form of distinct color associated with each element- Mg (red), Ca (blue), and P (green). It shows that the secondary phase particles in stir zone were composed of Ca and P elements (Fig. 3). Furthermore, the element mapping images also confirmed that the area faction of secondary particle within stir zone increased (1.64% ± 0.23, 5.10% ± 0.92, and 8.05% ± 1.24, respectively) with increasing added HA content. The observation along with XRD results (Fig. 2) further indicated that the additional HA content was successfully controlled and incorporated into the AZ31B matrix via FSP. More insights into microstructure evolution were obtained by observing the samples under TEM during the parallel work performed separately on these samples by the authors [21,31]. Bright field and dark field TEM microscopy coupled with the collection of SAD pattern revealed dispersion of HA particles within α-Mg grain with the particle size ranging from micrometer to nanometer scale. Since HA particles play a role in bio-reaction in the biological environment, the further biomineralization and biocompatibility evaluation and discussion relating to Mg-HA composites are presented in the following subsections.

3.3. Wettability

The quantification of three liquids contact angle and surface energy for as-received Mg and all FSP Mg-HA composites were listed in Table 2. The surface energy of as-received Mg was 37.92 mJ/m^2, and 5, 10, 20 wt%FSP Mg-HA composites exhibited higher surface energy values (43.02, 44.33, 46.81 mJ/m^2, respectively), indicating the increase of surface energy of AZ31B Mg alloy via FSP. Furthermore, it can be seen that the difference of surface energy between FSP Mg-HA composites was small. The results of SBF contact angle measurement clearly demonstrated that the FSP Mg-HA composites surface became more hydrophilic (contact angle range ≈ 45°–36°) compared to as-received Mg (≈50°) (Fig. 4). It can be noted that increase of added HA content further reduced the SBF contact angle, indicating the enhancement of surface wettability due to the presence of HA particles. In general, calcium being electrochemically active, the presence of HA facilitates heterogeneous nucleation within the metallic matrix and high energetic solid surface. Such a wetting favored surface is an important factor to determine the success of the implant-tissue integration [37]. To further understand the effects of enhanced wettability on the growth of apatite in vitro environment, the study of biomineralization is discussed in the following section.

3.4. Biomineralization

Previously, the biomineralization evaluation of as-received Mg and all FSP Mg-HA composites for various periods (1, 4, 8, and 12 days) of immersion in SBF was studied separately by the authors [31]. The optical microscopy observation during this former study, which have been conducted by the authors, showed evolution of various types of surface morphologies including the mineral deposit and corrosion pits [31]. Based on these observations, the samples in the longest period of 12 days immersion was considered due to the most promising mineral deposit layer formation compared to other immersed periods.

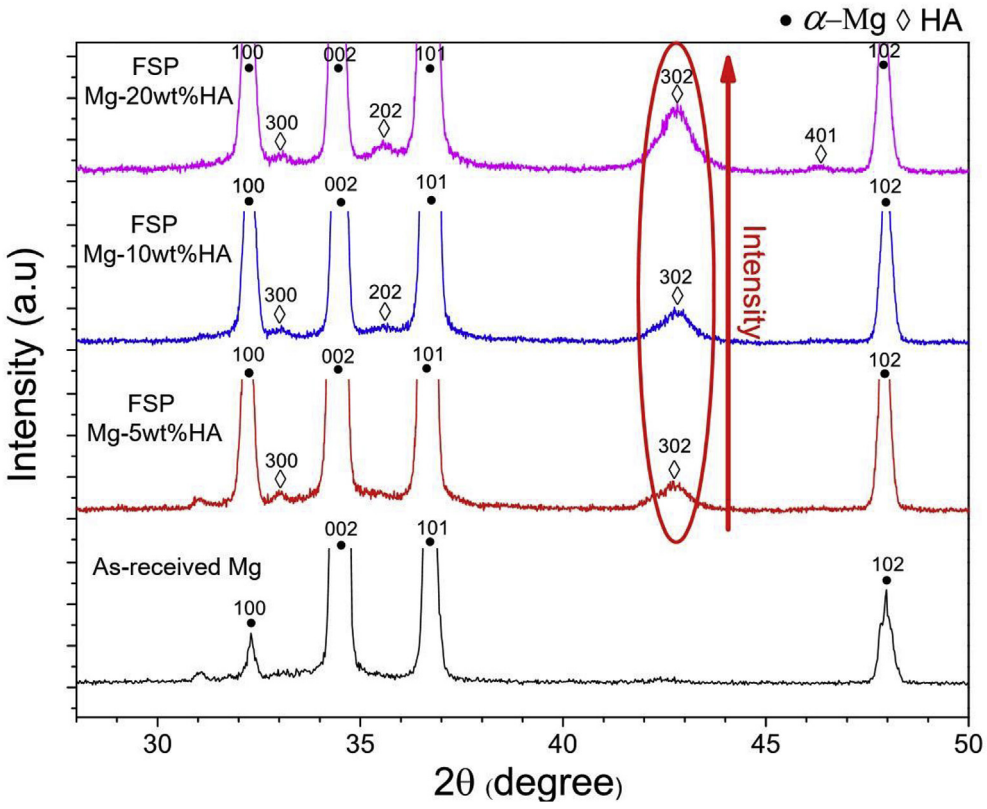

Fig. 2. XRD spectra corresponding to as-received Mg and all the FSP Mg-HA composites.

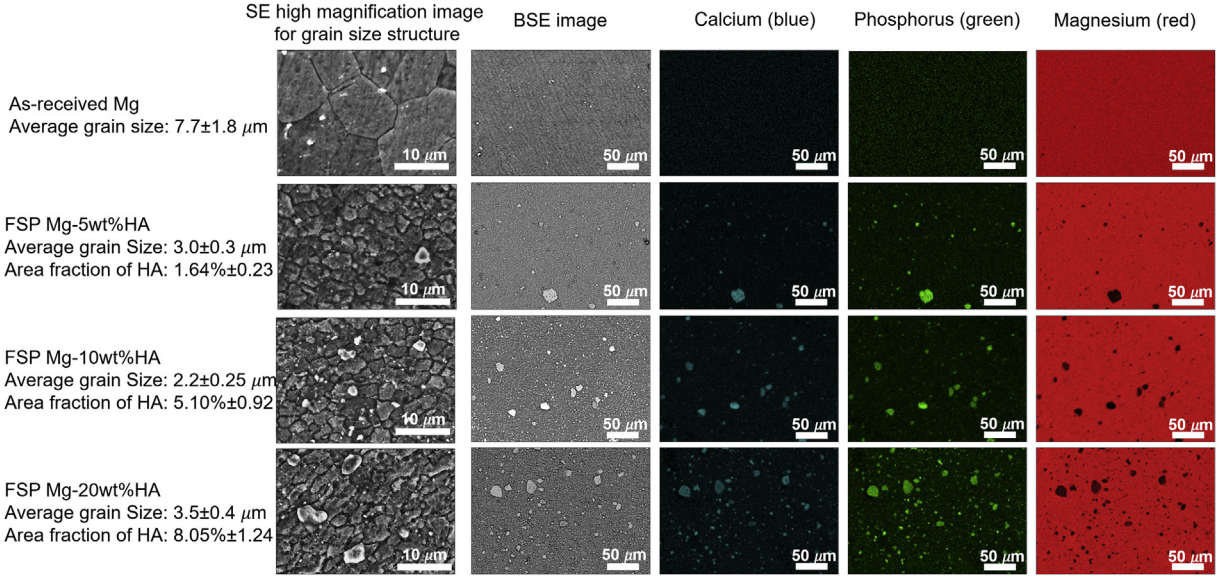

Fig. 3. SEM secondary electron mode, back scattering mode, and false-colored images of calcium (blue), phosphorus (green), and magnesium (red) elemental mapping images of as-received Mg and FSP Mg-5wt%, 10 wt%, and 20 wt%HA composites showing greatly refined microstructure after FSP. (For interpretation of the references to color in this figure legend, the reader is referred to the Web version of this article.)

Furthermore, there was no significant apatite morphology variation between different immersed period. Hence, the SEM image of 12 days immersed period was selected to represent not only as general but also long-term biomineralization characterization. Corresponding physical and compositional characteristics of these mineralized apatite characterized via SEM and the EDS are presented in Fig. 5. The mineral morphology of as-received Mg appeared to be a globular shape with petal-like surface structure (Fig. 5(a)). The corresponding EDS elemental analysis of the chemical composition of the mineral phases included Mg, O, Ca, and P elements. Different from as-received Mg, the mineralized phase which formed on all FSP Mg-HA samples were globular in morphology (Fig. 5 (b) to (d)) with same elements as detected on as-received Mg. The similar mineral morphology was also be reported by Sung et al. [38]. However, the results of EDS plots revealed that the predominant composition of mineralized surface of as-received Mg was Mg-based compound. Furthermore, in case of FSP Mg-HA

Table 2
The contact angle measurement and resultant total surface energy of as-received Mg and all FSP Mg-HA composites.

Processing condition	Contact angle measurement (degree)			Surface energy components (mJ/m^2)		Total surface energy (mJ/m^2)
	D.I Water	Formamide	1-Bromonaphthalene	γ^{LW}	γ^{AB}	γ^{Total}
As-received Mg	72.90 ± 3.01	59.60 ± 2.62	35.00 ± 2.12	36.70	1.22	37.92
FSP Mg-5wt%HA	49.50 ± 1.50	44.20 ± 5.19	18.20 ± 3.68	42.21	0.82	43.02
FSP Mg-10 wt%HA	49.20 ± 1.25	42.40 ± 3.44	21.00 ± 1.71	41.50	2.83	44.33
FSP Mg-20 wt%HA	48.50 ± 2.65	48.80 ± 2.09	16.71 ± 3.37	42.54	4.27	46.81

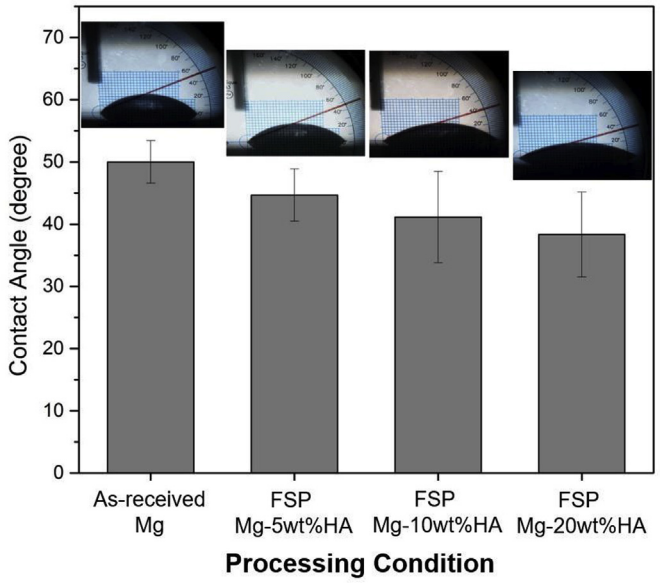

Fig. 4. The evaluation of surface wettability of as-received Mg and all FSP Mg-HA composites.

composites, the higher intensities of Ca and P suggested the presence of CaP-based mineral. It can be noted that the particle size of the mineral on FSP Mg-20 wt%HA (1.79 ± 0.20 μm) was finer than that on 5 wt% (4.66 ± 0.55 μm) and 10 wt% (4.25 ± 0.49 μm) composites. It might be attributed to the rapid apatite formation rate due to higher surface energy and improved wettability. Such the fine globular morphology may be the favorable structure for tissue integration during implantation.

The results of XPS analysis provided detailed information on chemical compounds and quantification of the elements in the mineral phase on the biomineralized samples (Fig. 6).

XPS spectra of all samples exhibited the presence of Mg 2p, Mg 2s, Mg KLL, Ca $2p_{1/2}$, Ca $2p_{3/2}$, P 2p, P 2s, O 2s, and O 1s peaks. The mineral phase on as-received Mg appeared to shift the binding energy of Mg 2p from 50.00 to 49.32 eV, signifying the tendency of formation of $Mg(OH)_2$ compound within the mineralized phase [39]. On the contrary, it is clearly shown that the Mg 2p peak for all FSP Mg-HA samples was low intensity peak with minimal shift in binding energy, indicating that the mineral phase was mainly constituted of CaP based phase. The P 2p plot also indicates that the existence of phosphate (PO^{3-}) compound within mineral of all biomineralized samples [40]. It is well known that Mg alloys are susceptible to corrosion in aqueous solution, resulting in formation of corrosion byproduct $Mg(OH)_2$ compound [8,41]. During immersion, large amount of Mg ions were released and then involved in the formation of mineral phase. This is likely to be the reason for formation of petal-like morphology on as-received Mg surface. On the other hand, the low degradation rate of FSP Mg-HA composites resulted in formation of the high Ca–P ration based apatite after biomineralization. Table 3 lists the semi-quantitatively derived Ca and P atomic concentrations and their ratio (Ca/P). Ca/P ratio range between 1.42 and 1.60 for FSP Mg-HA samples, and hence is very close to the Ca/P atomic ratio of stoichiometric HA (Ca/P:1.64) and tri-calcium phosphate (TCP, Ca/P:1.5) [17,42,43], This is indicative of the fact that FSP Mg-HA composite is highly preferable to form good quality of mineral phase suitable for implant application.

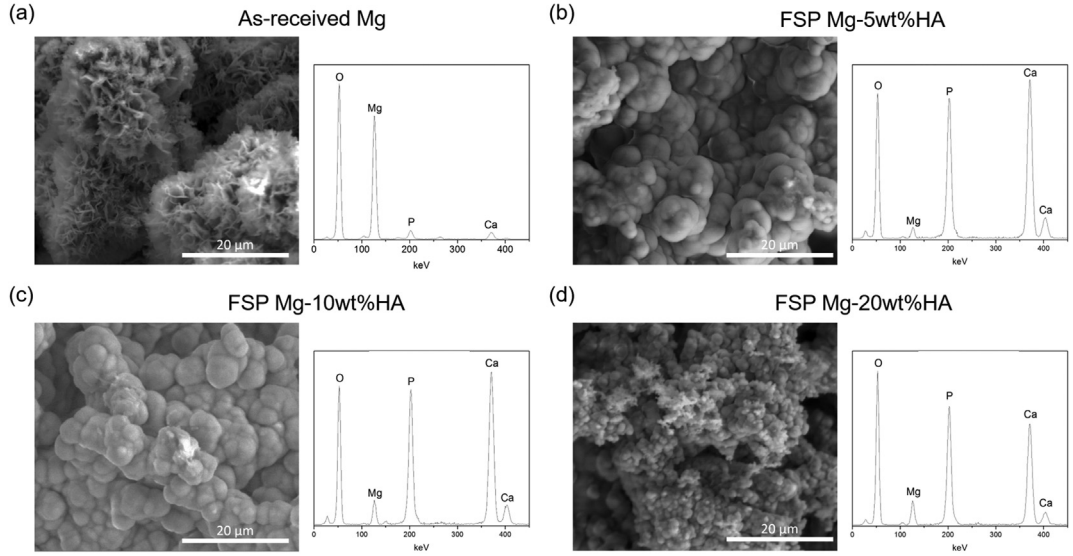

Fig. 5. SEM surface morphologies and corresponding EDS of the (a) as-received Mg, (b) FSP Mg-5wt%HA, (c) FSP Mg-10 wt%HA, and (d) FSP Mg-20 wt%HA after 12 days immersion in SBF.

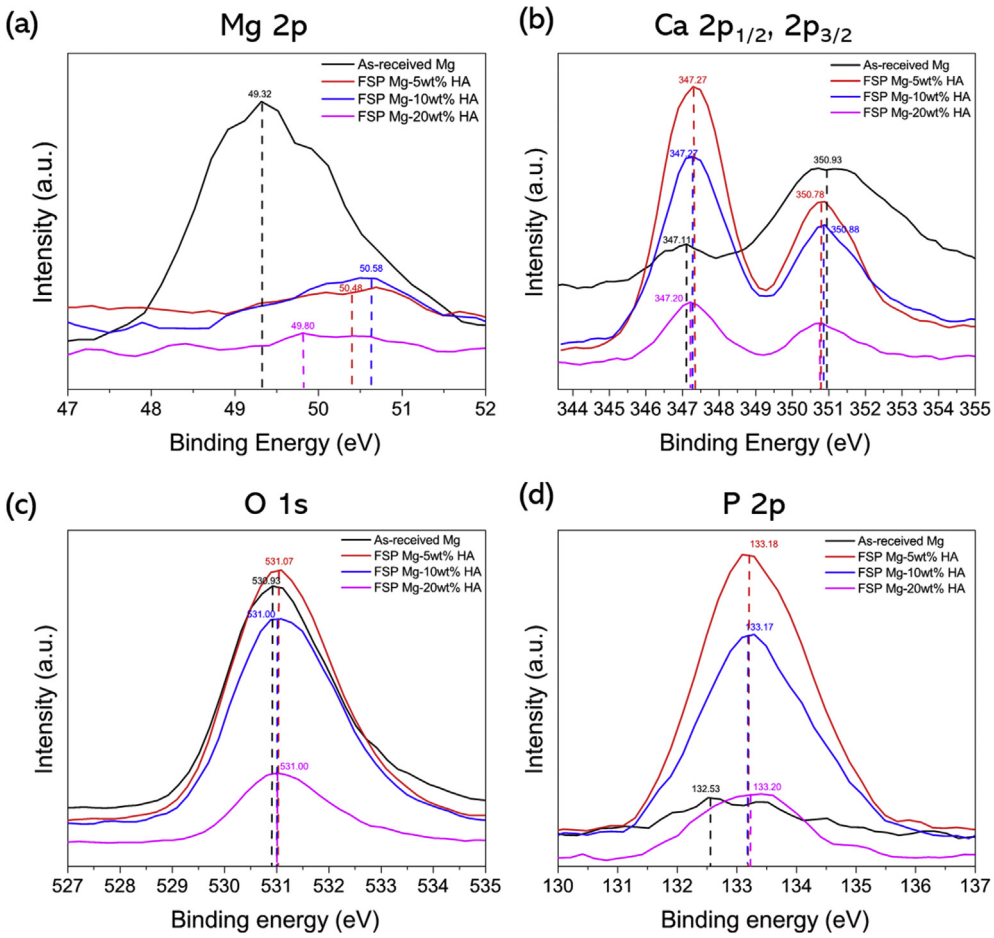

Fig. 6. XPS spectra of (a) Mg 2p, (b) Ca $2p_{1/2}$ and $2p_{3/2}$, (c) O 1s, and (d) P 2p elements of mineral apatite on as-received Mg and all FSP Mg-HA composites after biomineralization.

3.5. Hemocompatibility

The blood compatibility of as-received Mg and FSP Mg-HA composites were evaluated via platelet adhesion and hemolysis tests. As shown in Fig. 7(a), more adherent platelets were observed on as-received Mg than all FSP Mg-HA composites. In addition, the platelets formed aggregates on as-received Mg while few platelet aggregates were observed on FSP Mg-10 wt% and −20 wt%HA composites. The significant difference was also verified in the quantitative analysis of adhered platelets (Fig. 7(b)). Platelet adhesion, spreading and aggregation are considered to be a major mechanism of thrombosis [44]. These results indicated that the incorporation of HA particles provide an effective way to avoid thrombus formation of Mg alloys. Moreover, hemolysis, the damage of erythrocytes with the release of hemoglobin into the plasma, was examined. As shown in Fig. 7(c), the hemolysis ratios of all the groups were less than 5%, falling within the permissible limit for blood-contacting biomaterials according to ASTM F 756-08. These results suggested that embedding HA particles enhanced the blood compatibility of Mg alloys and the enhancement was a function of the HA content.

3.6. Biocompatibility

Cell compatibility is critical to implant biomaterials, and thus the cell biocompatibility on as-received Mg and all FSP Mg-HA composites was evaluated by MTT assay and cell counting. It was seen that cells cultured in FSP Mg-20 wt% showed significant higher values of cell viability and population after 1 and 7-day culture (Fig. 8(a) and (b)). On the other hand, the viability for as-received Mg and FSP Mg-5wt% and −10 wt%HA was similar after 1-day culture (Fig. 8(a)). After 7 days FSP Mg-10 wt%HA showed higher viability than as-received Mg. The cell counting results also showed higher cell population on FSP Mg-10 wt% and −20 wt%HA composites after 1 day and 7-day culture (Fig. 8(b)). These observations clearly showed that cell growth was promoted by the embedded HA particles via FSP, and increased as a function of the HA content in Mg matrix.

To understand how the HA content promoted cell growth, we examined the interactions between the cells and the substrates. The

Table 3
Elemental composition and semi-quantitative analysis of Ca and P in terms of atomic concentration for the as-received Mg and FSP Mg-HA composites.

Processing Condition	Elements present	Ca atomic concentration(%)	P atomic concentration(%)	Ca/P atomic ratio
As-received Mg	O, Mg, Ca, P	5.2	1.06	4.91
FSP Mg-5wt%HA	O, Mg, Ca, P	11.99	7.51	1.60
FSP Mg-10 wt%HA	O, Mg, Ca, P	9.8	6.89	1.42
FSP Mg-20 wt%HA	O, Mg, Ca, P	10.00	6.51	1.54

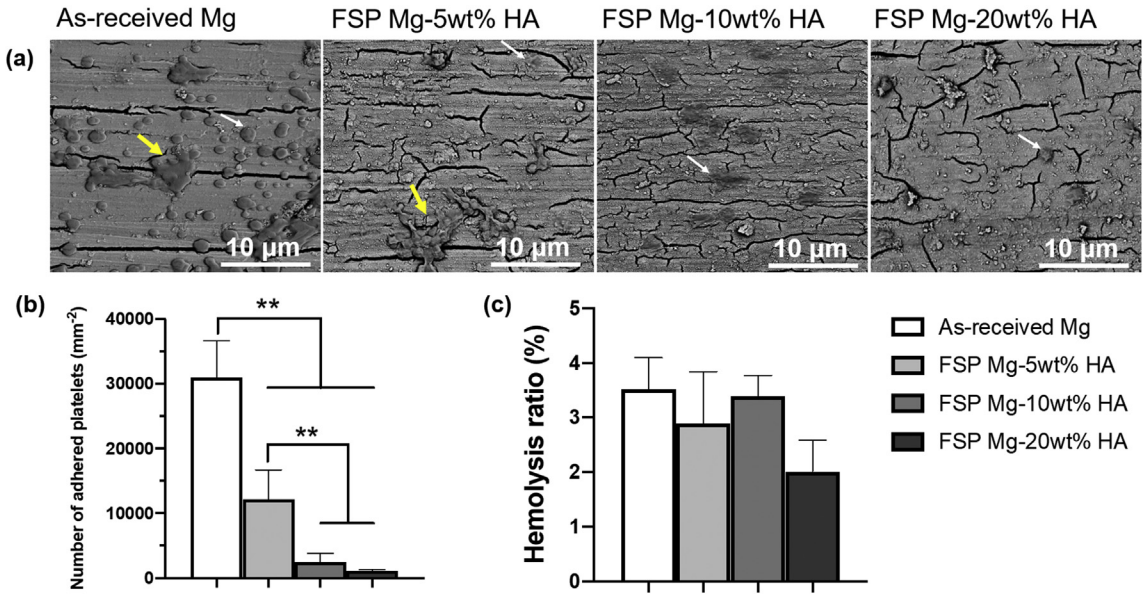

Fig. 7. Hemocompatibility of as-received Mg and FSP Mg-HA composites. (a) SEM images of adherent platelets on the samples. The white arrows indicated individual platelets and yellow arrowheads indicated platelet aggregates). (b) The corresponding number of adhered platelets. (c) Hemolysis ratio of different samples. **p < 0.01 between groups. (For interpretation of the references to color in this figure legend, the reader is referred to the Web version of this article.)

immunofluorescent images (Fig. 9) displayed that the cells on all FSP Mg-HA composites exhibited mature actin fibers, and the cells on FSP Mg-20 wt%HA composites showed prominent actin filament expression compared to as-received Mg, FSP Mg-5wt% and −10 wt%HA groups. The immunofluorescence observation indicated the cell adhesion was enhanced by the added HA particles, in particular the FSP Mg-20 wt% HA, being consistent with both cell viability and cell counting results.

The cell-substrate interactions were closely inspected via SEM imaging (Fig. 10). The low magnification images revealed that the cell density on all FSP Mg-HA composites was higher than as-received Mg. The cracks observed on all test samples after cell culture. These cracks were likely to be discontinuous oxide layer resulted from the heterogeneous stress distribution during cell culture. Moreover, the cells on as-received Mg showed round shape with limited spreading while the cells on FSP Mg-HA composites were spread and more extracellular matrix (ECM) (the high magnification images) secretion. Notably, the cells on FSP Mg-20 wt%HA displayed much larger cell area and more ECM deposition compare to other groups. The high magnification SEM image in BSE mode (Fig. 11) clearly showed the formation of filipodia on the HA grains, implying the HA grains facilitated the cell adhesion and spreading. Evidently, the presence of HA contents enhanced the cell adhesion and thus promoted cell growth. The resulted cell growth accelerated the secretion of ECM proteins, which further affected cell growth positively.

According to the collective data of wettability, biomineralization, blood compatibility, cell viability, cell morphology, and cell adhesion, it can be concluded that the microstructure evolution and addition of HA within the Mg matrix during FSP offer enhanced effects on both biomineralization and biocompatibility in vitro. In the present study, the SEM observation along with surface energy characterization revealed that the refined microstructural FSP Mg-HA composites exhibited higher surface energy and lower SBF contact angle compared to as-received Mg. The similar observation was reported by Sunil et al. that pure Mg and AZ31 alloy with smaller grain size possessed higher surface energy than the matrix with coarse grain structure [3,27]. In general, a grain boundary is an interface between grains, therefore due to the interfacial energy, the grain boundary area is more chemically active compared to grain interior. When the grain size of the matrix reduces, the fraction of grain boundary area with the surface becomes larger, resulting in enhancement of surface energy. In the present case, all FSP Mg-HA composites with various HA contents (5, 10, and 20 wt %) consisted of nearly same average grain size structure with a narrow variation in the surface energy values (43–48 mJ/m^2, Table 2). This is indicative of the fact that refined microstructure in FSP Mg-HA

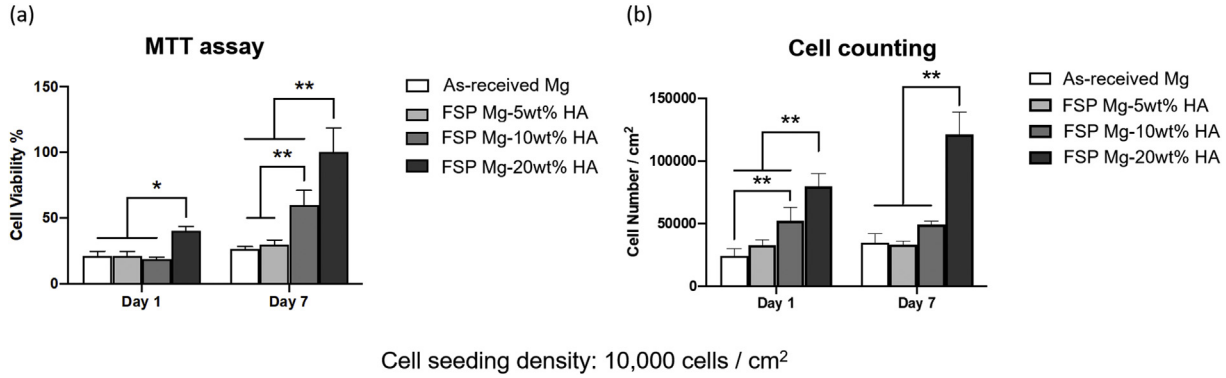

Fig. 8. The analyzed data of pre-osteoblasts (a) cell viability and (b) cell counting of as-received Mg and FSP Mg-HA composites after 1-day and 7-day culture. Cell viability data were normalized to the mean value of the data of FSP Mg-20 wt%HA groups.

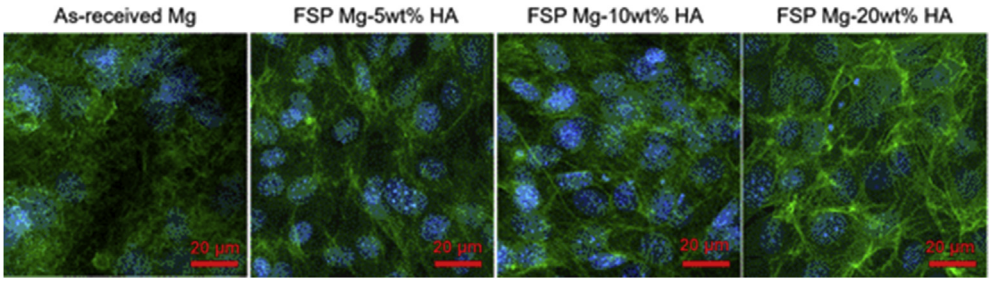

Fig. 9. The fluorescent images of pre-osteoblasts on as-received Mg and FSP Mg-HA composites after 1-day cell culture.

composites played the predominated factor in surface energy evolution. On the other hand, even though HA content (particles) appeared to have minimal effect on surface energy, the data of SBF contact angle measurement provided significantly higher hydrophilic tendency on higher HA content composites (Fig. 4). This may be attributed to two additional hydroxide bonds in HA chemical formula, leading to more hydroxide molecule absorption from SBF solution. Furthermore, the dispersion of HA in various particle sizes (scale range: μm to nm) not only reinforced the biomineralization, but also acted as a reactive site for cell grafting, adhesion, and growth due to their similar composition to the natural CaP mineral [45]. It is notable that surface wettability is not only affects biomineralization but also benefits to the cell spreading and reduces platelet adhesion. The platelet adhesion relies on the binding of fibrinogen on the material surface, and fibrinogen seems more ease to be absorbed on the surface of low wettability, which favors platelet aggregation [46–48]. As such, higher HA content composites promote blood compatibility, cell viability and cell spreading, indicating increased biocompatibility of these Mg-HA composites. Fig. 12 illustrates the relations between wettability, platelet adhesion, and cell growth. Before FSP, the AZ31B Mg alloy exhibits lower wettability, platelet aggregation, and limited cell growth (Fig. 12(a)). After FSP additive manufacturing, the novel features (refined microstructure and HA composites matrix) promote both wettability and cell spreading and inhibit the platelet adhesion (Fig. 12(b)). This demonstrate that FSP approach holds a promise in producing the suitable Mg-based biomaterial with improved biomineralization and biocompatibility. In light of this, the efforts are ongoing to investigate and extend the FSP parameters and processing strategies for larger composites matrix to fabricate promising property of orthopedic implant for healing and reformation of bone.

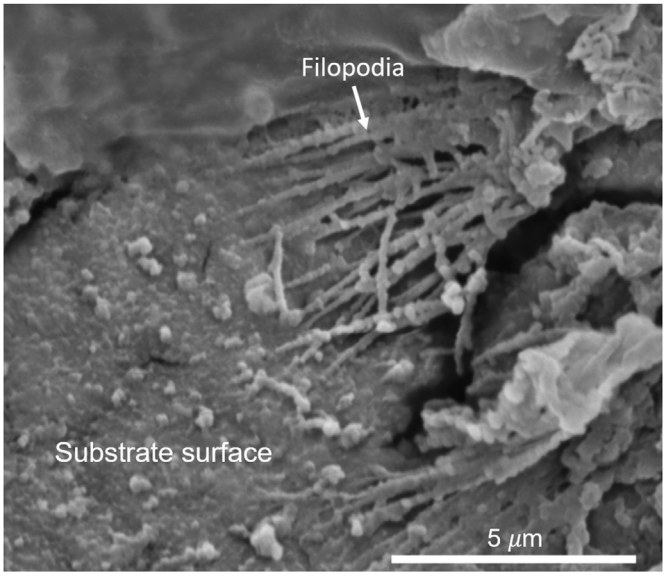

Fig. 11. Ultra-high magnification SEM images in BSE mode shows adhesion of pre-osteoblasts on FSP Mg-20 wt%HA composite surface after 1-day cell culture.

4. Conclusions

Mg-HA composites with varying HA content (5 wt%, 10 wt%, and 20 wt%) were additively produced using FSP technique. This process successfully resulted in mixing of HA in α-Mg matrix without forming secondary phase in the stir zone. Furthermore, the refined grain structure was obtained within the stir zone of Mg-HA composites

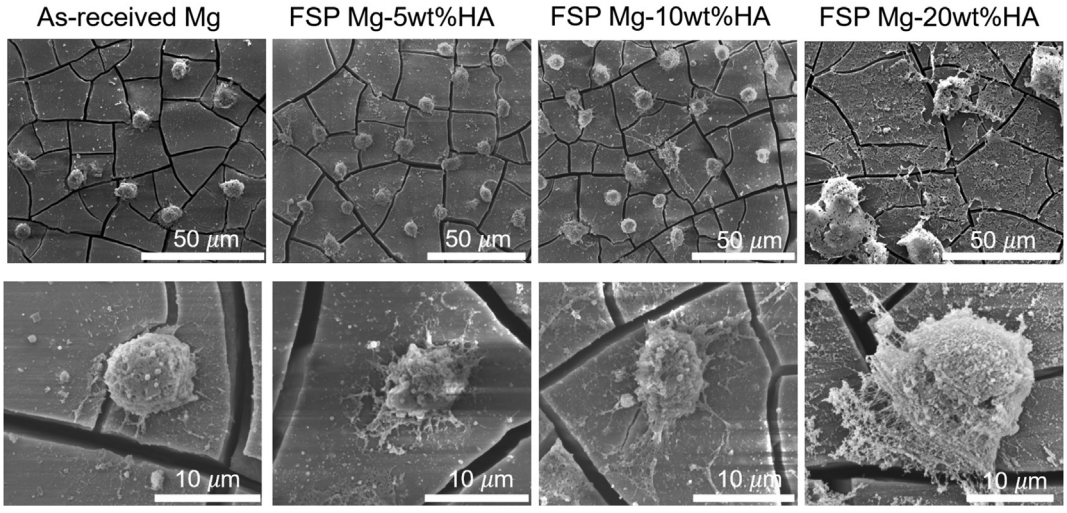

Fig. 10. Low and high magnification SEM images of pre-osteoblasts on as-received Mg and FSP Mg-HA composites after 1-day cell culture.

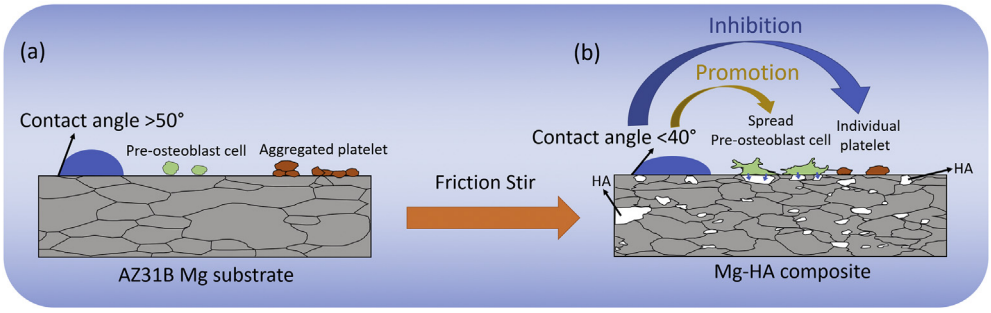

Fig. 12. Schematic diagram demonstrates the improvement of wettability, cell viability, and platelet adhesion on FSP Mg-HA composites compared to as-received Mg.

(average grain size in the range of 2.2 ± 0.25 μm to 3.5 ± 0.4 μm) compared to the as-received AZ31B Mg alloy (average grain size 7.76 ± 1.78 μm). In addition, the dispersion of HA with various size-scale was presented uniformly within the stir zone of Mg-HA composites. The combined influence of refined microstructure and HA dispersion in Mg matrix benefited the biomineralization and biocompatibility of FSP Mg-HA composites. The highest surface energy was obtained on FSP Mg-20 wt%HA composite (46.81 mJ/m^2) compared to the as-received Mg (37.92 mJ/m^2). The Ca/P ratio in the mineral phase (range:1.54 to 1.60) close to nature bone (1.64), indicating the favorable biomineralization property for tissue integration. All FSP Mg-HA composites possessed improved hemocompatibility, biocompatibility and cell adhesion compared to as-received AZ31B Mg alloy. Hence, this novel friction stir additively manufactured process can be utilized as a promising technique to develop Mg based composites for biodegradable implant application.

CRediT authorship contribution statement

Yee-Hsien Ho: Methodology, Investigation, Writing - original draft. **Kun Man:** Methodology, Investigation, Formal analysis, Writing - original draft. **Sameehan S. Joshi:** Methodology, Writing - review & editing. **Mangesh V. Pantawane:** Writing - review & editing. **Tso-Chang Wu:** Investigation. **Yong Yang:** Supervision, Validation, Writing - review & editing. **Narendra B. Dahotre:** Supervision, Conceptualization, Writing - review & editing.

Declaration of competing interest

None.

Acknowledgment

The authors acknowledge the Materials Research Facility (MRF) at the University of North Texas for access to microscopy and phase analysis facilities.

References

[1] G. Song, S. Song, A possible biodegradable magnesium implant material, Adv. Eng. Mater. 9 (4) (2007) 298–302.
[2] M.P. Staiger, A.M. Pietak, J. Huadmai, G. Dias, Magnesium and its alloys as orthopedic biomaterials: a review, Biomaterials 27 (9) (2006) 1728–1734.
[3] B.R. Sunil, A.A. Kumar, T.S. Kumar, U. Chakkingal, Role of biomineralization on the degradation of fine grained az31 magnesium alloy processed by groove pressing, Mater. Sci. Eng. C 33 (3) (2013) 1607–1615.
[4] X.-N. Gu, Y.-F. Zheng, A review on magnesium alloys as biodegradable materials, Front. Mater. Sci. China 4 (2) (2010) 111–115.
[5] N. Erdmann, N. Angrisani, J. Reifenrath, A. Lucas, F. Thorey, D. Bormann, A. Meyer-Lindenberg, Biomechanical testing and degradation analysis of mgca0. 8 alloy screws: a comparative in vivo study in rabbits, Acta Biomater. 7 (3) (2011) 1421–1428.
[6] Y. Xin, K. Huo, H. Tao, G. Tang, P. K. Chu, Influence of aggressive ions on the degradation behavior of biomedical magnesium alloy in physiological environment, Acta Biomater. 4 (6).
[7] R. Zeng, W. Dietzel, F. Witte, N. Hort, C. Blawert, Progress and challenge for magnesium alloys as biomaterials, Adv. Eng. Mater. 10 (8) (2008) B3–B14.
[8] G.L. Song, A. Atrens, Corrosion mechanisms of magnesium alloys, Adv. Eng. Mater. 1 (1) (1999) 11–33.
[9] Y. Ding, C. Wen, P. Hodgson, Y. Li, Effects of alloying elements on the corrosion behavior and biocompatibility of biodegradable magnesium alloys: a review, J. Mater. Chem. B 2 (14) (2014) 1912–1933.
[10] N. Sezer, Z. Evis, S.M. Kayhan, A. Tahmasebifar, M. Koç, Review of magnesium-based biomaterials and their applications, J. Magnes. Alloys. 6 (1) (2018) 23–43.
[11] S.S.A. El-Rahman, Neuropathology of aluminum toxicity in rats (glutamate and gaba impairment), Pharmacol. Res. 47 (3) (2003) 189–194.
[12] Y. Nakamura, Y. Tsumura, Y. Tonogai, T. Shibata, Y. Ito, Differences in behavior among the chlorides of seven rare earth elements administered intravenously to rats, Toxicol. Sci. 37 (2) (1997) 106–116.
[13] J.R. Jones, D.S. Brauer, L. Hupa, D.C. Greenspan, Bioglass and bioactive glasses and their impact on healthcare, Int. J. Appl. Glass Sci. 7 (4) (2016) 423–434.
[14] P.-H. Kuo, S. S. Joshi, X. Lu, Y.-H. Ho, Y. Xiang, N. B. Dahotre, J. Du, Laser coating of bioactive glasses on bioimplant titanium alloys, Int. J. Appl. Glass Sci.. 10 (3) 2019 307-320.
[15] V. Orlovskii, V. Komlev, S. Barinov, Hydroxyapatite and hydroxyapatite-based ceramics, Inorg. Mater. 38 (10) (2002) 973–984.
[16] T. Albrektsson, C. Johansson, Osteoinduction, osteoconduction and osseointegration, Eur. Spine J. 10 (2) (2001) S96–S101.
[17] S.R. Paital, N.B. Dahotre, Calcium phosphate coatings for bio-implant applications: materials, performance factors, and methodologies, Mater. Sci. Eng. R Rep. 66 (1) (2009) 1–70.
[18] C. Wen, S. Guan, L. Peng, C. Ren, X. Wang, Z. Hu, Characterization and degradation behavior of az31 alloy surface modified by bone-like hydroxyapatite for implant applications, Appl. Surf. Sci. 255 (13-14) (2009) 6433–6438.
[19] F.-z. Cui, J.-x. Yang, Y.-p. Jiao, Q.-s. Yin, Y. Zhang, I.-S. Lee, Calcium phosphate coating on magnesium alloy for modification of degradation behavior, Front. Mater. Sci. China 2 (2) (2008) 143–148.
[20] Y. Song, D. Shan, E. Han, Electrodeposition of hydroxyapatite coating on az91d magnesium alloy for biomaterial application, Mater. Lett. 62 (17) (2008) 3276–3279.
[21] Y.-H. Ho, S.S. Joshi, T.-C. Wu, C.-M. Hung, N.-J. Ho, N.B. Dahotre, In-vitro biocorrosion behavior of friction stir additively manufactured az31b magnesium alloy-hydroxyapatite composites, Mater. Sci. Eng. C (2020) 110632.
[22] T.-C. Wu, Y.-H. Ho, S.S. Joshi, R.S. Rajamure, N.B. Dahotre, Microstructure and corrosion behavior of laser surface-treated az31b mg bio-implant material, Laser Med. Sci. 32 (4) (2017) 797–803.
[23] F. Witte, F. Feyerabend, P. Maier, J. Fischer, M. Störmer, C. Blawert, W. Dietzel, N. Hort, Biodegradable magnesium–hydroxyapatite metal matrix composites, Biomaterials 28 (13) (2007) 2163–2174.
[24] K.A. Khalil, A.A. Almajid, Effect of high-frequency induction heat sintering conditions on the microstructure and mechanical properties of nanostructured magnesium/hydroxyapatite nanocomposites, Mater. Des. 36 (1980-2015) (2012) 58–68.
[25] A.K. Khanra, H.C. Jung, S.H. Yu, K.S. Hong, K.S. Shin, Microstructure and mechanical properties of mg-hap composites, Bull. Mater. Sci. 33 (1) (2010) 43–47.
[26] B.R. Sunil, C. Ganapathy, T.S. Kumar, U. Chakkingal, Processing and mechanical behavior of lamellar structured degradable magnesium–hydroxyapatite implants, J. Mech. Behav. Biomed. Mater. 40 (2014) 178–189.
[27] B.R. Sunil, T.S. Kumar, U. Chakkingal, V. Nandakumar, M. Doble, Friction stir processing of magnesium–nanohydroxyapatite composites with controlled in vitro degradation behavior, Mater. Sci. Eng. C 39 (2014) 315–324.
[28] N. Kalakuntla, N. Bhatia, S. Patel, S.S. Joshi, T.-C. Wu, Y.-H. Ho, N.B. Dahotre, Laser patterned hydroxyapatite surfaces on az31b magnesium alloy for consumable implant applications, Materialia (2020) 100693.
[29] M.B. Kannan, W. Dietzel, R. Zettler, In vitro degradation behaviour of a friction stir processed magnesium alloy, J. Mater. Sci. Mater. Med. 22 (11) (2011) 2397–2401.
[30] B.R. Sunil, T.S. Kumar, U. Chakkingal, V. Nandakumar, M. Doble, Nano-hydroxyapatite reinforced az31 magnesium alloy by friction stir processing: a solid state processing for biodegradable metal matrix composites, J. Mater. Sci. Mater. Med. 25 (4) (2014) 975–988.
[31] Y.-H. Ho, In Vitro Corrosion Behavior of Magnesium Alloy Az 31b-Hydroxyapatite

Metallic Matrix Composites Processed via Friction Stir Processing, Doctoral Dissertation University of North Texas, Denton TX, 2016.
[32] C. Van Oss, R. Good, M. Chaudhury, Additive and nonadditive surface tension components and the interpretation of contact angles, Langmuir 4 (4) (1988) 884–891.
[33] S.R. Paital, Z. Cao, W. He, N.B. Dahotre, Wetting effects on in vitro bioactivity and in vitro biocompatibility of laser micro-textured ca-p coating, Biofabrication 2 (2) (2010) 025001.
[34] S. Bargir, S. Dunn, B. Jefferson, J. Macadam, S. Parsons, The use of contact angle measurements to estimate the adhesion propensity of calcium carbonate to solid substrates in water, Appl. Surf. Sci. 255 (9) (2009) 4873–4879.
[35] Y.-H. Ho, H.D. Vora, N.B. Dahotre, Laser surface modification of az31b mg alloy for bio-wettability, J. Biomater. Appl. 29 (7) (2015) 915–928.
[36] Z. Ma, Friction stir processing technology: a review, Metall. Mater. Trans. 39 (3) (2008) 642–658.
[37] C.J. Wilson, R.E. Clegg, D.I. Leavesley, M.J. Pearcy, Mediation of biomaterial–cell interactions by adsorbed proteins: a review, Tissue Eng. 11 (1-2) (2005) 1–18.
[38] B.R. Sunil, T.S. Kumar, U. Chakkingal, V. Nandakumar, M. Doble, V.D. Prasad, M. Raghunath, In vitro and in vivo studies of biodegradable fine grained az31 magnesium alloy produced by equal channel angular pressing, Mater. Sci. Eng. C 59 (2016) 356–367.
[39] S. Ardizzone, C. Bianchi, M. Fadoni, B. Vercelli, Magnesium salts and oxide: an xps overview, Appl. Surf. Sci. 119 (3-4) (1997) 253–259.
[40] M. Biesinger, X-ray Photoelectron Spectroscopy (Xps) Reference Pages, (2015).
[41] G. Song, Control of biodegradation of biocompatable magnesium alloys, Corrosion Sci. 49 (4) (2007) 1696–1701.
[42] L. Ellies, D. Nelson, J. Featherstone, Crystallographic changes in calcium phosphates during plasma-spraying, Biomaterials 13 (5) (1992) 313–316.
[43] H. Liu, H. Yazici, C. Ergun, T.J. Webster, H. Bermek, An in vitro evaluation of the ca/p ratio for the cytocompatibility of nano-to-micron particulate calcium phosphates for bone regeneration, Acta Biomater. 4 (5) (2008) 1472–1479.
[44] M. Alehosseini, N. Golafshan, M. Kharaziha, M. Fathi, H. Edris, Hemocompatible and bioactive heparin-loaded pcl-α-tcp fibrous membranes for bone tissue engineering, Macromol. Biosci. 18 (6) (2018) 1800020.
[45] L. Bacakova, E. Filova, M. Parizek, T. Ruml, V. Svorcik, Modulation of cell adhesion, proliferation and differentiation on materials designed for body implants, Biotechnol. Adv. 29 (6) (2011) 739–767.
[46] F. Gao, Y. Hu, G. Li, S. Liu, L. Quan, Z. Yang, Y. Wei, C. Pan, Layer-by-layer deposition of bioactive layers on magnesium alloy stent materials to improve corrosion resistance and biocompatibility, Bioact. Mater. 5 (3) (2020) 611–623.
[47] W.-B. Tsai, J.M. Grunkemeier, C.D. McFarland, T.A. Horbett, Platelet adhesion to polystyrene-based surfaces preadsorbed with plasmas selectively depleted in fibrinogen, fibronectin, vitronectin, or von willebrand's factor, J. Biomed. Mater. Res. 60 (3) (2002) 348–359.
[48] L. Zhang, B. Casey, D.K. Galanakis, C. Marmorat, S. Skoog, K. Vorvolakos, M. Simon, M.H. Rafailovich, The influence of surface chemistry on adsorbed fibrinogen conformation, orientation, fiber formation and platelet adhesion, Acta Biomater. 54 (2017) 164–174.